

Model Driven Design for Flexure-Based Microrobots

Neel Doshi, Benjamin Goldberg, Ranjana Sahai, Noah Jafferis, Daniel Aukes, and Robert J. Wood
 Harvard University, John A. Paulson School of Engineering and Applied Sciences, Cambridge, MA, USA

Abstract— This paper presents a non-linear, dynamic model of the flexure-based transmission in the Harvard Ambulatory Microrobot (HAMR). The model is derived from first principles and has led to a more comprehensive understanding of the components in this transmission. In particular, an empirical model of the dynamic properties of the compliant Kapton flexures is developed and verified against theoretical results from beam and vibration theory. Furthermore, the fabrication of the piezoelectric bending actuators that drive the transmission is improved to match theoretical performance predictions. The transmission model is validated against experimental data taken on HAMR for the quasi-static (1-10 Hz) operating mode, and is used to redesign the transmission for improved performance in this regime. The model based redesign results in a 266% increase in the work done by the foot when compared to a previous version of HAMR. This leads to a payload capacity of 2.9g, which is $\sim 2 \times$ the robot's mass and a 114% increase. Finally, the model is validated in the dynamic regime (40-150 Hz) and the merits of a second order linear approximation are discussed.

Index Terms— Dynamic models, Legged microrobots, Biologically Inspired Robots, Compliant Flexures, Piezoelectric actuators

I. INTRODUCTION

Recent advances in the manufacturing of articulated, millimeter-scale structures in [1] has enabled the development of highly complex, dynamic insect-scale robots. Exemplary devices include flapping wing micro air vehicles [2], and legged robots that are capable of high speed locomotion [3], turning [4], climbing [5], and obstacle traversal [6].

Research in legged robots at larger scales utilize dynamic models ([7],[8],[9],[10]) to demonstrate even greater capabilities in running and climbing ([11],[12]). This is in part due to the accurate understanding of the individual components (e.g. motors, springs, bearings, etc).

However, only quasi-static models (e.g., powertrain selection in [13]) exist for insect-scale crawling robots. This is due to the complexity of the transmission used to map the motion of the actuators to the leg, unknown dynamic properties (stiffness and damping) of the compliant flexures used as joints in these robots, and a poor understanding of the piezoelectric actuators relative to electromagnetic motors. One exception is the hybrid-dynamic model developed in [4] to understand the behavior of an underactuated centipede inspired millirobot. This model, however, does not capture the dynamics of the robot near its resonance and was only validated in the quasi-static regime.

Due to the complexity of the devices designed using the PC-MEMS process [1], better models are needed to allow for faster and more informed design iterations. Models developed from first principles provide insight into the behavior

of the components of the system – in this case the compliant flexures and actuators – and increase the ability to model systems that utilize similar materials and manufacturing techniques.

More specifically to the insect-scale crawling robot described in this paper, a dynamic model can further improve the speed, climbing and efficiency by being able to simulate device operation and predict system behavior. These performance metrics are important for potential applications in search and rescue, hazardous environment exploration, and inspection tasks well suited for insect-scale robots.

This paper outlines a method for modeling flexure based microrobots using the transmission of the Harvard Ambulatory Microrobot (HAMR) as an example. In section II we describe the structure of the model, and in sections III and IV we discuss lumped parameter models for the actuators and compliant flexures respectively. We verify the model in the quasi-static regime (1 – 10 Hz) and use the model to redesign the transmission for improved performance at low frequencies in section V. Model predictions are also compared with the dynamic behavior of the robot's transmission in section VI.

II. MODEL OF TRANSMISSION

A dynamic model of HAMR's transmission is developed in *MotionGenesis* [14], a symbolic software that numerically solves the dynamics of physical systems. Fig. 1 shows the linkages of the transmission and definitions used in the model. The model has two inputs and two states: the blocked forces (inputs) and deflections (states) of the lift and swing actuators: F_b^l , F_b^s , δ^l , and δ^s . F_b is the blocked force, δ is the deflection, and the superscripts l and s indicate lift and swing actuators, respectively. The lift and swing actuators are optimal energy density piezoelectric bending actuators described in [15] and more recently characterized in [16]. Each actuator is modeled as a force source (F_b) in parallel with a serial stiffness (k_a) as in [15]. The determination of $F_b^{\{s,l\}}$ and $k_a^{\{s,l\}}$ is explained in section III and is shown to follow the model presented in [16] after a number of design iterations. The effective mass and damping of the actuator as discussed in [17] were initially incorporated in the model but were found to be negligible. Lower transmission ratios coupled with high operational frequencies, however will likely require actuator mass effects to be reconsidered.

The model has two output degrees of freedom (DOFs): the position of the leg tip in the z and x directions (d_l and d_s , respectively). The deflection of the actuator tip is linearized by a compliant Kapton flexure. The crank-sliders

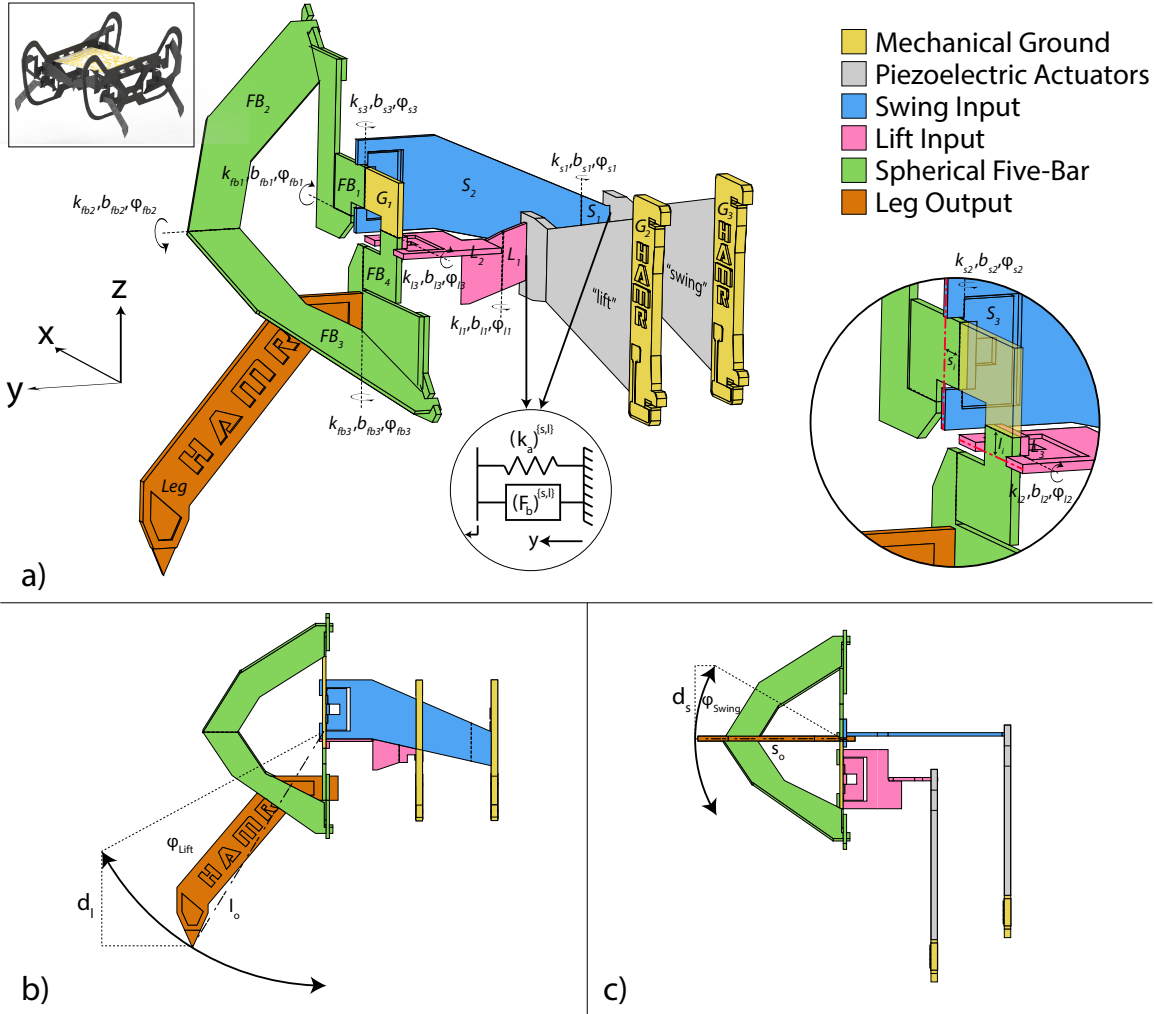


Fig. 1. Model of the HAMR transmission in isometric (a), lift/front (b), and swing/top (c) perspectives. Actuator deflection is mapped to the leg (orange) through a crank-slider mechanism, shown in pink for the lift and blue for the swing. The green spherical five-bar serves to decouple the two inputs: the lift actuator controlling z motion and the swing actuator controlling x motion. Full body Solidworks model shown in top left corner.

(pink and blue) convert the linearized motion of the actuators to a rotary motion and amplify the actuator displacement by the transmission ratio $T_l^* = l_0/l_i$ for lift and $T_s^* = s_0/s_i$ for swing. However, since only the z component of the lift output is useful, we redefine the lift transmission ratio to be $T_l = s_0/l_i$. The swing transmission ratio T_s is the same as T_s^* . As investigated in [18], the spherical five-bar (SFB) allows the system to be analyzed as two separate single-input, single-output systems in the quasi-static regime.

The crank-sliders and the SFB are two parallel linkages comprised of eleven rigid bodies connected to each other and mechanical ground via nine compliant Kapton flexures. Each rigid body is assigned physical dimensions, a mass, an inertia, and a center of mass position in its local frame. These quantities were determined using a Solidworks model with mass properties and dimensions informed by measurements taken on the HAMR. The Kapton flexures are modeled as one-dimensional pin joints as in [19]. They are assumed to be loaded in pure bending, and their dynamic properties are described by a torsional stiffness and damping. The stiffness and damping for these flexures is determined using a combination of beam theory and experimentally determined

equations, discussed in section IV.

Kane's method was used to write the equations of motion for HAMR's transmission in *MotionGenesis*. The velocity of the actuators, $\dot{\delta}^l$ and $\dot{\delta}^s$, were defined as the generalized velocities and nine kinematic equations (defined in Appendix A) were derived to constrain the position and velocities of the nine DOFs introduced by the Kapton flexures in terms of δ^l , δ^s , and the generalized velocities. Equations (9) and (10) define ψ_{l2} and ψ_{s2} , the angular deflections of flexures l_2 and s_2 , respectively. Two more equations (11) enforce the loop constraint for the lift crank-slider by defining the position of the flexure l_2 that rotates by ψ_{l2} to be the same when approached from mechanical ground on the transmission (G_1) or the actuator (G_2). Two more equations (12) enforce the loop constraint for the swing crank-slider in the same manner. The last three equations (13-15) are the loop constraint for the SFB. These are enforced by constraining the orientation of a virtual frame $[\hat{v}_x, \hat{v}_y, \hat{v}_z]$ (not depicted) that undergoes rotations by $\psi_{s3}, \psi_{fb1}, \psi_{fb2}, \psi_{fb3}$, and ψ_{l3} to be the same as the orientation of the Newtonian frame (i.e. mechanical ground).

Given this information, *MotionGenesis* numerically in-

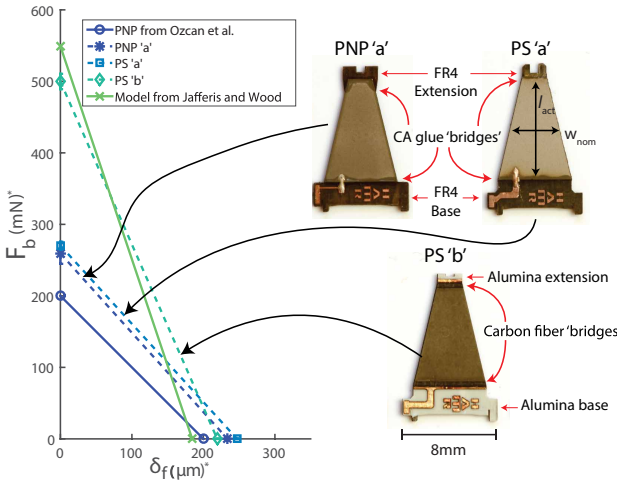


Fig. 2. Piezoelectric actuator energy curve when driven at 225V (left). Images of three different actuator versions compared in this section and relevant geometric parameters (right).

* indicates that values are peak one-way.

TABLE I
ACTUATOR PARAMETERS

Parameter	Old Geometry	New Geometry
PZT Thickness (μm)	135	135
CF Thickness (μm)	110	55
PZT Length (mm)	8.8	9.2
Nominal Width (mm)	4.2	3.5
Extension Length (mm)	0.8	1
Width Ratio	1.5	1.5
δ_f (μm)	184*, 219 \pm 5.6†	300*, 314 \pm 6.9†
F_b (mN)	549*, 500 \pm 10.7†	320*, 320 \pm 4.4†
D_u (J/kg)	0.46*, 0.50 \pm 0.02†	0.52*, 0.54 \pm 0.01†

*Based on the model in [16].

†Mean experimental measurements \pm s.d. with n=4 at 225V drive

tegrates the dynamics of the transmission from a valid kinematic state, which is determined by solving the non-linear constraints given values of δ^l , δ^s , $\dot{\delta}^l$, and $\dot{\delta}^s$.

III. ACTUATORS

The design of the actuators used in HAMR-VP [13] is improved to increase performance and match the theory presented in [16]. Matching the model in [16] allows for accurate estimates of $F_b^{(s,l)}$ and $k_a^{(s,l)}$ which enables rapid iterations on actuator design without fabrication and testing.

Two manufacturing methods, ‘pick and place’ (PNP) and ‘pre-stacked’ (PS), for piezoelectric actuators are compared to improve the energy density of the actuators. The PNP method cures the composite actuator after the raw materials are individually machined. The PS method described in [16] machines the actuator geometry after curing a bulk actuator composite laminate. The baseline geometry used for the actuators is from Ozcan et al. and is shown in Table I.

The free deflection and blocked force are measured using a 225V peak-to-peak sinusoidal drive signal at a frequency of 1Hz. The amplitude and frequency is chosen for convenience of analysis as it has been shown in [16] that blocked force scales approximately linearly with voltage in our operating regime (50 – 225 V) and is approximately constant over the

TABLE II
SUMMARY OF ACTUATOR PERFORMANCE METRICS

	m_a (mg)	δ_f (μm)*	F_b (mN)*	D_u (J/kg)	sample size
PNP† from [13]	96	200	200	0.21	n/a
PNP† ‘a’	100	234	259	0.32	n=4
PS‡ ‘a’	100	247	270	0.35	n=4
PS‡ ‘b’	109	219	500	0.5	n=4
Model from [16]	109	184	549	0.46	n/a

* indicates peak one-way values.

†PNP refers to the manual ‘pick and place’ method of placing materials in the actuator fabrication.

‡PS refers to the ‘pre-stacked’ method of material placement described in [16].

frequencies of interest (1 – 150 Hz). Force data is recorded on a 6-axis force/torque sensor (ATI Nano-17Ti) and free deflection is recorded using a camera and vision tracking (PixeLINK PL-B741F and Xcitex-ProAnalyst). The base of the actuator is clamped in a reusable aluminum mount. Compared to previous methods in [13], this clamp reduces parasitic bending at the base of the actuator. Furthermore it is shown in [16] that parasitic compliance can also occur if the interface between the base and the PZT plate is not reinforced. These two improvements are made to the actuators from [13] and are shown in the PNP ‘a’ of Fig. 2. The PS ‘a’ and ‘b’ actuators in Fig. 2 are both machined from a pre-cured composite laminate, the difference being that, as in [16], PS ‘b’ uses an alumina base and tip (instead of FR4) and has carbon fiber (instead of CA glue) ‘bridges’ at the PZT-Alumina interface. The free deflection of these improved actuators is 219 μm and the blocked force is 500 mN. A full summary of the actuators discussed is shown in Table II.

The energy density of the actuators is calculated as the area under the force-displacement curve shown in Fig. 2.

$$D_u = \frac{\delta_f F_b}{2m_a} \quad (1)$$

This convention is chosen to represent the energy available from the actuator to act on the HAMR transmission. Note that this value is scaled by a factor of $\frac{1}{4}$ compared to [15] and [16] to more appropriately describe operation of the HAMR transmission which can be approximated as a linear spring load in the quasi-static regime.

Since the PS ‘b’ actuators maximize energy density and agree with the model from Jafferis et al., this fabrication method is used in the design of future actuators. In particular, we re-size the actuators in section V-B using the model in [16]. These actuators are described as the new geometry actuators in Table I. This type of redesign was previously not possible as there was no theoretical framework explaining the behavior of the PNP ‘a’ and PS ‘a’ actuators.

IV. FLEXURE MODEL

There are three primary types of compliant flexures employed in the design of multi-layer composite microrobots: uncastellated flexures, castellated flexures and mirrored-castellated flexures (see Fig. 3). Adding castellations creates a more well defined axis of rotation and increases the

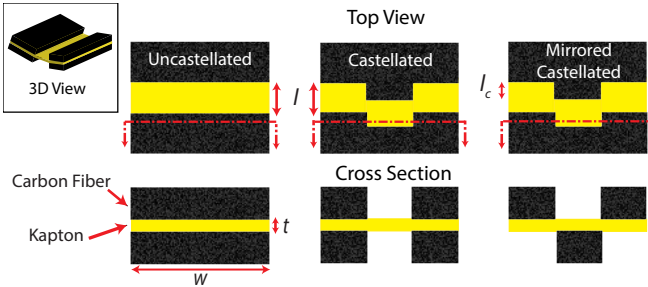


Fig. 3. The top row depicts a top view of three different flexure designs used in microrobots. The bottom row represents the cross section taken at the indicated dotted red lines. A perspective view of an uncastellated flexure is shown on the left.

stiffness of the flexure while maintaining the same maximum deflection from the uncastellated case. These compliant flexures can be approximated as small-length flexural pivots and are assumed to be loaded in pure bending (see [20] for details). The bending stiffness of uncastellated flexures can be estimated theoretically from simple beam theory, as shown in Eq. 2:

$$k = \frac{E_k w t^3}{12l} \quad (2)$$

E_k is the Young's modulus of Kapton (2.5 GPa) [21], w is the width of the flexure, t is the thickness, and l is the length. These dimensions are defined in Fig. 3. We hypothesize that the stiffness of castellated hinges will have a similar form to Eq. 2 for some effective length, $l_{eff} : l - l_c \leq l_{eff} \leq l$, where l_c is the castellation length defined in Fig. 3.

In the following subsections, we experimentally validate Eq. 2 for the stiffness of uncastellated Kapton flexures and develop a theoretical formula for the torsional damping constant of uncastellated flexures. These two equations determine a map between an uncastellated flexure's geometry and its dynamic properties that can be used to inform design. We also determine l_{eff} for the mirrored-castellated flexures used in HAMR, which vary only in width.

A. Experimental flexure characterization

We use the motion of a damped harmonic oscillator (a physical pendulum) with the Kapton flexure of interest as the pivot to determine the stiffness (k) and damping (b) for the flexure. This test is preferable to a static force/deflection experiment because we can determine b from the decay envelope of the oscillation. The experimental setup is shown in Fig. 4. An electromagnet is energized, and holds the pendulum. A servo then moves the electromagnet and pendulum along the arc anchored by the center of the flexure to an initial angle between 5 and 15 degrees. The magnet is de-energized and a high speed camera (Phantom Miro M/R/LC310) is triggered to capture the motion of the pendulum. This procedure ensures that the oscillations remain small, that off-axis loading is minimized, and that the initial velocity of the pendulum is zero. Note that the experiments were run in a vacuum of 24 in-Hg to eliminate the effect of aerodynamic damping. Though this experimental setup is an improvement over static force/deflection tests, there are a few

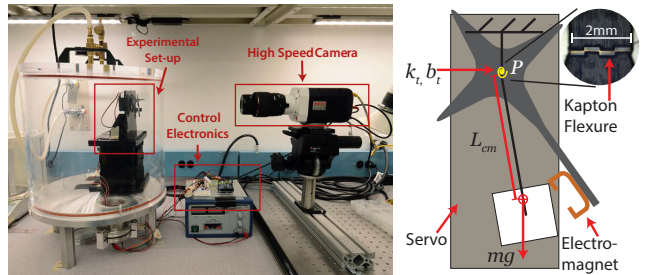


Fig. 4. Experimental setup (left) and schematic of experiment initial conditions (right).

limitations that will be addressed in future work. Namely, we can only study the hinge behavior at the natural frequency of pendulum and for small angles; therefore, we cannot fully span the range of actuation frequencies for HAMR and we cannot determine k or b for large deflections.

Since the angle of oscillation is kept small, the motion of the pendulum is described by a linear ordinary differential equation in its angle. From this equation, we can extract experimental values for stiffness (k_m) and damping (b_m).

$$b_m = 2\zeta\omega_n I_p \quad (3)$$

$$k_m = I_p \omega_n^2 - mgL_{cm} \quad (4)$$

Here, ζ is the damping ratio, ω_n is the natural frequency, g is the acceleration due to gravity, I_p is the inertia of the pendulum about the pivot (center of flexure), m is the mass of the pendulum, and L_{cm} is the distance between the pivot and the center of mass. The mass related quantities were obtained from a Solidworks model of the pendulum. The frequency of oscillation (ω_d) was obtained by finding the average time between vertical crossings of the oscillating pendulum, where the position was determined using vision-based tracking. A least squares fit to the logarithm of decaying oscillation amplitudes was used to find decay rate (σ). The natural frequency is then $\sqrt{\sigma^2 + \omega_d^2}$ and the damping ratio is σ/ω_n .

B. Results

We tested 25 different uncastellated flexure geometries varying in width from 0.8 mm to 6 mm, varying in length from 30 μ m to 2 mm, and for four different Kapton thicknesses: 7.5 μ m, 12 μ m, 25 μ m, and 50 μ m. We took at least two trials per flexure, and the data displayed is the average of these trials. Since Kapton is a polymer, we expected it to exhibit visco-elastic behavior that would manifest itself in terms of a frequency dependent damping constant. In particular, we expect it to follow the formula for a frequency dependent dashpot given in [22], that is

$$b(\omega) = \frac{k\eta(\omega)}{\omega} = \frac{\eta(\omega)E_k w t^3}{12l\omega} \quad (5)$$

Here $\omega = \omega_d$ is the frequency of oscillation of the pendulum, and $\eta(\omega)$ is the frequency dependent lost tangent of the material. We approximate $\eta(\omega)$ with a single value η . The results from these experiments are shown in Fig. 5. We normalized k_m by

$$y = \frac{12l}{t^3} k_m \quad (6)$$

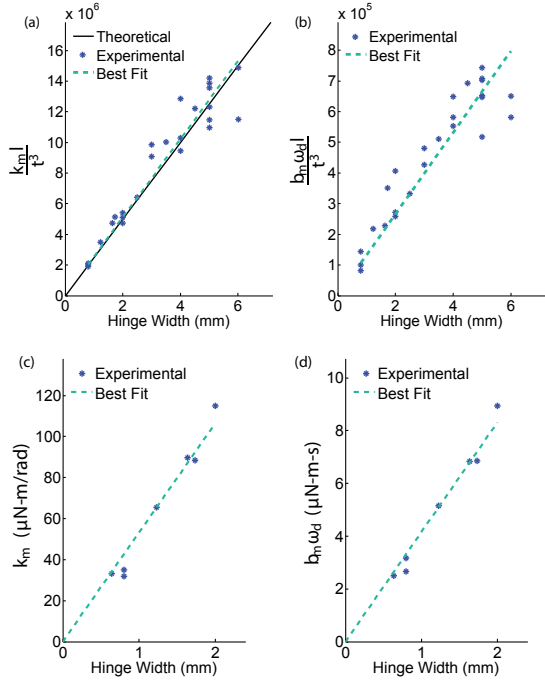


Fig. 5. Flexure test results. Best fits for stiffness (a) and damping (b) for uncastellated hinges ($n=25$). Best fit for stiffness (c) and damping (d) for mirrored-castellated hinges used in HAMR’s transmissions ($n=7$).

causing the data to collapse onto a line of the form $y = (E_k)_m w$, where $(E_k)_m$ is the experimentally determined Young’s modulus of Kapton. We obtained the best fit in the least squares sense, with R-squared value equal to 0.90 and $(E_k)_m = 2.56 \text{ GPa}$ (2.3% different from the value in [21]). Similarly, we normalized b_m by

$$z = \frac{12l\omega_d}{t^3} b_m \quad (7)$$

Once again, the data collapsed onto a line of the form $z = \eta_m (E_k)_m w$, where η_m is our experimental estimate of the loss tangent. The R-squared value of this fit is 0.83, and we calculated $\eta_m = 0.05$ using the value of $(E_k)_m$ determined above. The value of η_m is within the range of loss factors for polymers: 0.01 – 0.1 [23].

In addition, we tested the castellated flexures used in HAMR. All nine of these flexures were mirrored-castellated, $25 \mu\text{m}$ thick, $120 \mu\text{m}$ long with $100 \mu\text{m}$ long castellations, and the width was varied between 0.8 mm and 2 mm to achieve different stiffness and damping. We took at least two trials per flexure, and the data shown in Fig. 5 is the average of these trials. Since the only variation was in width, k_m was not normalized before plotting against width. The R-squared value of the best fit was 0.96. We used $(E_k)_m$ and Eq. (2) to determine that the effective length of these hinges was of $l_{eff} = 66 \mu\text{m}$. We normalized b_m by w_d and plotted it against width. We found the line of best fit with R-squared equal to 0.97. We used Eq. (5), $(E_k)_m$, l_{eff} to determine $\eta'_m = 0.08$, again within the range for polymers. Note that η_m is not exactly equal to η'_m because the loss tangent is generally a function of frequency and the mean frequency of oscillation ($\sim 31 \text{ rps}$) for the seven HAMR hinges is different from that of the 25 uncastellated hinges ($\sim 40 \text{ rps}$).

TABLE III
FLEXURE VALUES USED IN MODEL

Hinge	$w(\text{mm})$	$k_m \dagger (\mu\text{N}\cdot\text{m}/\text{rad})$	$b_m \omega_d \dagger (\mu\text{N}\cdot\text{m}\cdot\text{s})$
S1	1.74	88.4	6.8
S2	0.80	35.0	3.2
S3, FB3	0.64	33.3	2.5
L1	1.64	89.8	6.8
L2	0.80	31.9	2.7
L3, FB1	1.23	65.4	5.2
FB2	2.00	115.0	8.9

[†] Values determined from experimental lines of best fit and using Eqs. (2) and (5) with $l_{eff} = 66 \mu\text{m}$ and $\eta'_m = 0.08$.

The empirical best fits are used in the transmission model to determine the damping and stiffness of the nine Kapton flexures and these values are shown in Table III. Though we do not explore the effects of varying length, thickness, or the castellation geometry on l_{eff} , we now quantitatively understand how to achieve a specific stiffness and damping for mirrored-castellated flexures by varying the width.

The experimental process and equations described in this section can be used to understand the dynamic properties of small-length flexural pivots, and the specific experimental fits derived are valid for a wide range of Kapton flexural pivots.

V. QUASI-STATIC MODEL VALIDATION AND REDESIGN

The transmission model developed in sections II-IV is validated against experimental data taken from HAMR transmissions and is used to improve the robot’s performance. Two versions of HAMR are considered. HAMR-V2.0 has the same transmission as HAMR-VP from Baisch et al., however, the swing DOFs are no longer contralaterally coupled. This enabled full characterization of a single transmission before considering the effect of swing DOF coupling. The newest version of HAMR (described in section V-B) is based on the model and is referred to as HAMR-VI.

A. Quasi-static Validation

The model was validated against two HAMRV-2.0 and HAMR VI transmissions in the quasi-static regime (1 – 10 Hz) using two different criteria: the trajectory of the foot, and the transmission’s static force/deflection curves.

The data for the foot trajectory is recorded using a camera and vision tracking (Phantom v7.3 and Xcitex-ProAnalyst). The stiffness and damping constants for the Kapton flexures used in this transmission are listed in Table III, the lift transmission ratio (T_l) is 16.5 ($T_l^* = 30.8$), and the swing transmission ratio (T_s) is 20.5. The geometric and mass properties of the 11 linkages are omitted for brevity. These transmissions were outfitted with the PS ‘a’ actuators, and driven by 1 Hz 225V peak-to-peak sinusoidal signal. The tips of both actuators were offset $50 \mu\text{m}$ in the negative y direction in the model to reflect the pre-load placed on the transmission during assembly as explained in [13].

The result from this test is shown in the top row of Fig. 6. The model (in blue) closely matches the experimental data (in dashed-cyan) for the swing DOF shown in (d), and slightly over-predicts the experimental data for the lift DOF (c). The lift transmission does not achieve the predicted

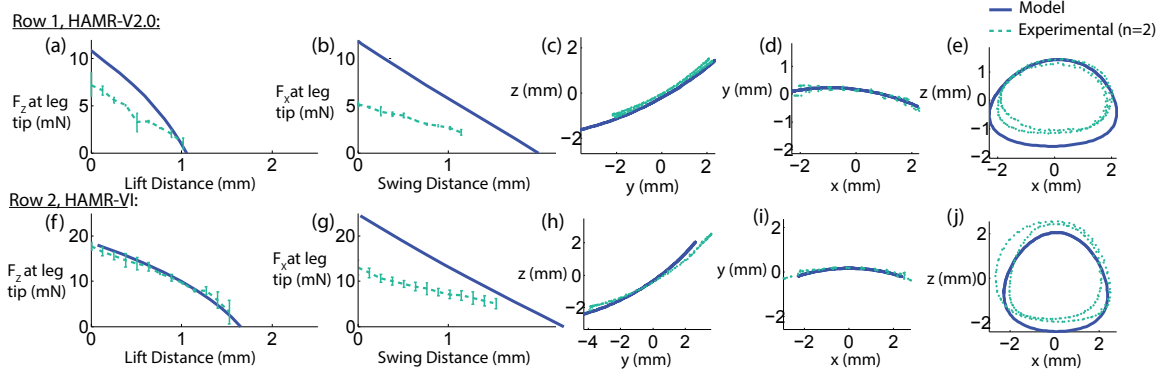


Fig. 6. Quasi-static force versus deflection curves (a,b,f,g). Foot trajectory for lift (c,h), swing (d,i), and both actuated 90° out of phase (e,j). Model predictions are shown in blue, and experimental data ($n=2$) are in cyan. Top row is HAMR-V2.0 transmissions, and bottom row is HAMR-VI transmissions.

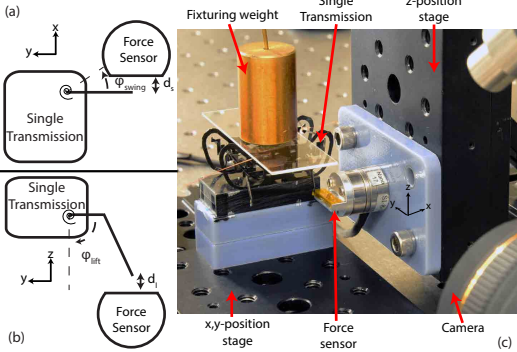


Fig. 7. Schematic of swing (a) and lift (b) force-deflection tests. Experimental setup (c).

displacement due to losses caused by small misalignments during fabrication that result in changes in stiffness that are magnified by the square of the high transmission ratio (T_l^*).

The experimental force/deflection curves were obtained by placing the 6-axis force/torque sensor (ATI Nano-17Ti) on a micro-manipulation stage directly adjacent to the leg for the swing tests or under the leg for the lift tests as shown in Fig. 7. The lift (or swing) DOF of the leg was then actuated using a 0.5 Hz 225 V peak-to-peak sinusoidal signal and the maximum force in z (or x) was recorded as F_z (or F_x) in addition to the position of the force sensor, d_l (or d_s). The micro-manipulation stage was then moved away in increments of $127\mu\text{m}$, and the test was repeated until no force was measured. There was a significant off-axis (y) force exerted by the foot ($\sim 30\%$ of the on-axis force) on the sensor for both the lift and the swing test. Thus, the model curves were determined by applying both an on-axis force and the appropriate y force.

The results are shown in Fig. 6(a) for the lift and Fig. 6(b) for the swing. The lift transmission provided slightly less force than the model prediction because of the aforementioned losses due to misalignments. The swing transmission, however, provided almost 50% less force than predicted. This is because the off-axis (y) force from the sensor places a twist moment on the swing flexures s_3 and fb_3 (as opposed to the bending moment placed on l_3 and fb_1). These flexures twist under this load as the ratio of the twist stiffness (given in [24]) to the bending stiffness (Eq. 2) of a compliant flexure is fundamentally limited by Eq. 8.

$$k_{twist} = \frac{2}{1 + \nu} \quad (8)$$

Here ν is the Possion's ratio (0.34 for Kapton) [21], and the ratio is equal to ≈ 1.5 for compliant Kapton flexures. Since the moment arm for the y force is about 1.5 times longer than that for the x force, the hinge undergoes a significant twist deformation that reduces the x force at the foot for the swing. This deformation, however, is not captured by the model as we choose to approximate the flexures as single DOF (bending) pivots, leading to flexures that are infinitely stiff in the twist direction.

B. Model-based redesign

Based on the improvements made to the actuators in section III and the discovery that s_3 and fb_3 were twisting when loaded, we chose to resize the transmission to improve performance in the quasi-static regime. From Fig. 8 we can see that for a given actuator, work done by the foot over one cycle increases as the transmission ratio (T) decreases. The blocked force (not depicted) at the foot is inversely proportional to the transmission ratio as expected; however, the free deflection does not increase linearly with the transmission ratio. This is because the effective stiffness of the transmission in the actuator frame increases by the square of the transmission ratio and counteracts the linear increase in deflection.

Thus, we tried to minimize the transmission ratio, which can be thought of impedance matching for the infinite load provided by the ground when HAMR is walking. The length of the actuators was constrained to < 10 mm to avoid major design changes, and the free deflection and actuator mass of HAMR-V2.0's actuators were maintained.

The redesigned transmission used the “new geometry” prestack actuators described in Table I. T_l was reduced to 12 ($T_l^* = 22.4$), and T_s was reduced to 13. The stiffness of s_3 and fb_1 was doubled by increasing the width to counteract the twisting motion mentioned in section V-A. This robot, named HAMR-VI, was built and the experimental results were compared against model predictions for the two tests mentioned in section V-A. The results from the leg trajectory and force/deflection tests are shown in the bottom row Fig. 6, and serve as another point of comparison for the model.

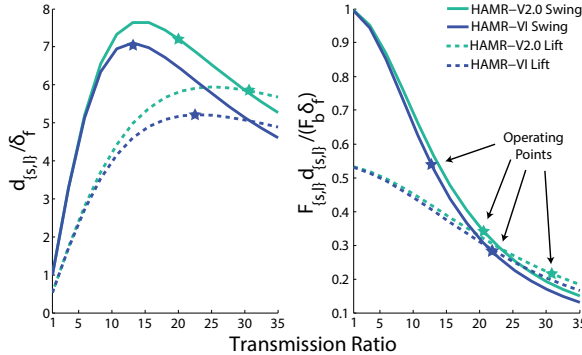


Fig. 8. Model prediction for varying the transmission ratio for a given actuator size. Cyan lines are for HAMR-V2.0 using the PS ‘a’ actuators, and blue lines for HAMR-VI are using the new geometry PS ‘b’ actuators. Dashed and solid represent the lift and swing DOF, respectively. The stars indicate the chosen transmission ratio for each case.

TABLE IV
HAMR-VI VERSUS HAMR-V2.0

HAMR	$d^\dagger(\text{mm})$	$F^\dagger(\text{mN})$	$F_d(\mu\text{J})$	$F_d/F_b\delta_f$
V2.0 - Lift	1.3 ± 0.2	7.2 ± 1.3	9.4 ± 2.2	0.14 ± 0.2
V2.0 - Swing	2.1 ± 0.2	5.2 ± 0.3	10.1 ± 1.2	0.17 ± 0.02
VI - Lift	2.2 ± 0.1	17.7 ± 0.8	38.9 ± 2.5	0.38 ± 0.04
VI - Swing	2.5 ± 0.3	13.0 ± 1.6	32.5 ± 5.6	0.31 ± 0.02

Data are mean experimental measurements ($n=2$) with \pm s.d.

\dagger Maximum one-way values for a single cycle

The experimental foot trajectory for both DOFs and the lift force/deflection curve match the model as reducing T_l^* and T_s has made robot less susceptible to manufacturing errors. The force exerted by the swing suffers from the same issues discussed in section V-A. Doubling stiffness of s_3 and f_{b3} was offset by the a doubling of the x and y forces.

HAMR-VI performance demonstrates that the model was used to drastically improve the transmission in the quasi-static regime. The two robots are compared in Table IV.

C. Payload Carrying Performance

The force data from section V-B suggests that the payload carrying capacity of HAMR-VI should increase by more than a factor of two since the individual leg lift force increased from 7.2mN to 17.7 mN. Payload tests are performed by adding discrete weights on top of the robot and running HAMR at gait frequencies up to 10 Hz. The average velocity of the robot is tracked using an overhead camera and visual tracking (Phantom v7.3 and Xcitex-ProAnalyst) and is summarized in Fig. 9. The gait and the driving scheme used is consistent with the tests in [3] which uses a trot and a 200 V peak-to-peak drive signal. These experiments demonstrate that HAMR-VI is capable of carrying 2.9 g. The maximum payload capacity is increased by 1.6 g from HAMR-V2.0 to HAMR-VI, a 114% increase normalized by percentage of the body weight with the nominal weights for HAMR-V2.0 and HAMR-VI being 1.41 g and 1.44 g, respectively. Note that the percent increase is only 91% compared to HAMR-VP from [3] since the nominal weight of HAMR-VP is 1.23 g, but it has the same payload carrying capacity as HAMR-V2.0.

Locomotion at all frequencies and payloads with HAMR-

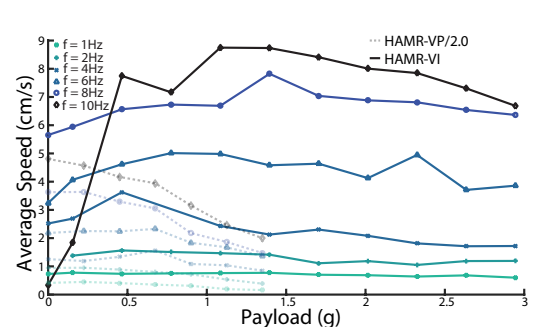


Fig. 9. Payload tests for HAMR-VP and HAMR-VI at 200V in the quasi-static regime. Each curve depicts HAMR’s speed versus weight for different quasi-static actuation frequencies. Payload results from HAMR-VP (Baisch et al.) shown in faded, dashed lines.

VI is faster than HAMR-V2.0 with the exception of unloaded and minimally loaded trials at 10 Hz actuation frequencies. This is due to the body dynamics which causes the robot to bounce and inhibits forward locomotion. In HAMR-VP, this transition to instability occurred only at frequencies greater than 10 Hz. The reason for this shift is likely due to the increased leg force and deflection which causes an earlier transition to these dynamic effects. A full high speed characterization is left to future work where the presented dynamic model will be extended to a dynamic walking model.

VI. DYNAMIC VALIDATION

We validated the model in the dynamic regime for HAMR. Evidence from [3] suggests that the dynamics of the transmission can be approximated as that of two decoupled, second order, linear, single input, single-output systems, allowing us to represent each with a bode plot. Therefore we compare the frequency response of two HAMR-V2.0 and HAMR-VI transmissions against the model. The transmissions were driven by a linear chirp between 1 – 130Hz for HAMR-V2.0 and 1 – 140Hz for HAMR-VI at voltages between 50 and 60V. The position of the foot is recorded using a camera and vision tracking (Phantom v7.3 and Xcitex-ProAnalyst), and the results are shown in Fig. 10.

The model accurately predicts the resonant frequency of the lift DOF transmissions. The predicted swing resonant peak, however, is at a higher frequency due to the twist loads placed by the inertia of the leg on hinges s_3 and f_{b3} . The model over-estimates the quality factor for both the lift and the swing DOFs. This is most likely due to the fact that the η'_m for the Kapton flexures was estimated for frequencies between 1 – 10 Hz. Since η'_m is a function of frequency, these estimates are less accurate near resonance.

Overall, the model represents the high frequency dynamics of the robot well. The shape of the bode plots show that the transmission can be represented well by two SISO second order systems (lift and swing) that map drive voltage (linearly related to actuator F_b) to displacement (δ) at the foot.

VII. CONCLUSION

A dynamic model of the HAMR transmission is developed from first principles and is compared against experimental

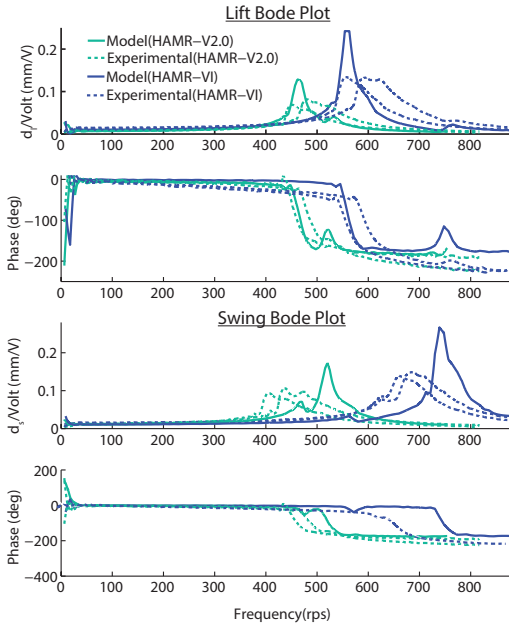


Fig. 10. Bode plots for the lift (top) and swing (bottom)

data. This model is used to inform the design of HAMR-VI, which outperforms HAMR-V2.0 in the quasi-static regime in terms of work done by the foot, speed, and payload capacity. More generally, we present a method for modeling flexure based microrobots and demonstrate that such models are useful in understanding and modifying the behavior of these complex robots. Furthermore, the methods and equations used to characterize the Kapton flexures can be used to characterize flexural pivots made from different materials, and the specific fits presented can be used as design and analysis tools by those working with Kapton flexures.

This work, however, is just a first step towards a more complete understanding of these flexure-based microrobots. Future work includes characterizing the behavior of the Kapton flexures at higher frequencies and larger angles using a dynamometer. We also intend to use the design principles outlined in section V-B to define a formal optimization to maximize transmission efficiency. Finally, the extended goal is to incorporate this model into a full-body locomotion model for HAMR that can be used for design and control in both the quasi-static and dynamic regimes.

APPENDIX A

$$\psi_{l2} = \psi_{l3} - \psi_{l1} \quad (9)$$

$$\psi_{s2} = \psi_{s3} - \psi_{s1} \quad (10)$$

$$\vec{l}_{G1 \rightarrow l_2} - \vec{l}_{G2 \rightarrow l_2} = \vec{0} \quad (11)$$

$$\vec{l}_{G1 \rightarrow s_2} - \vec{l}_{G2 \rightarrow s_2} = \vec{0} \quad (12)$$

$$\hat{v}_x \cdot \hat{x} - 1 = 0 \quad (13)$$

$$\hat{v}_y \cdot \hat{y} - 1 = 0 \quad (14)$$

$$\hat{v}_z \cdot \hat{z} - 1 = 0 \quad (15)$$

ACKNOWLEDGMENTS

This work is partially funded by the Wyss Institute for Biologically Inspired Engineering, the National Science

Foundation, and National Defense Science and Engineering Graduate Fellowship. Any opinion, findings, and conclusions or recommendations expressed in this material are those of the authors and do not necessarily reflect the views of the National Science Foundation.

REFERENCES

- [1] J. P. Whitney, P. S. Sreetharan, K. Y. Ma, and R. J. Wood, "Pop-up book MEMS," *Journal of Micromechanics and Microengineering*, vol. 21, no. 11, p. 115021, 2011.
- [2] K. Y. Ma, P. Chirarattananon, S. B. Fuller, and R. J. Wood, "Controlled Flight of a Biologically Inspired, Insect-Scale Robot," *Science*, vol. 340, no. 6132, pp. 603–607, 2013.
- [3] A. T. Baisch, O. Ozcan, B. Goldberg, D. Ithier, and R. J. Wood, "High speed locomotion for a quadrupedal microrobot," *The International Journal of Robotics Research*, p. 0278364914521473, 2014.
- [4] K. Hoffman and R. Wood, "Turning gaits and optimal undulatory gaits for a modular centipede-inspired millirobot," in *4th IEEE RAS/EMBS Conf. on Biomedical Robotics and Biomechatronics (BioRob)*, Rome, Italy, 2012, pp. 1052–1059.
- [5] B. Seitz, B. Goldberg, N. Doshi, O. Ozcan, D. Christensen, E. Hawkes, C. Mark, and R. J. Wood, Robert J.and Full, "Bio-inspired mechanisms for inclined locomotion in a legged insect-scale robot," *Under Review - ROBIO*, 2014.
- [6] K. L. Hoffman and R. J. Wood, "Robustness of centipede-inspired millirobot locomotion to leg failures," in *Intelligent Robots and Systems (IROS), 2013 IEEE/RSJ International Conference on*. IEEE, 2013, pp. 1472–1479.
- [7] M. H. Raibert, *Legged robots that balance*. The MIT Press, Cambridge, MA, 1985.
- [8] M. Buehler, "Dynamic locomotion with one, four and six-legged robots," DTIC Document, Tech. Rep., 2005.
- [9] S. A. Bailey, J. G. Cham, M. R. Cutkosky, and R. J. Full, "Comparing the locomotion dynamics of the cockroach and a shape deposition manufactured biomimetic hexapod," in *Experimental Robotics VII*. Springer, 2001, pp. 239–248.
- [10] P. Birkmeyer, A. G. Gillies, and R. S. Fearing, "Dynamic climbing of near-vertical smooth surfaces," in *IEEE/RSJ Intl. Conf. on Intelligent Robots and Systems (IROS), Vilamoura, Portugal*, 2012.
- [11] BostonDynamics, "CHEETAH - Fastest Legged Robot," http://www.bostondynamics.com/robot_cheetah.html, 2013.
- [12] P. Birkmeyer, K. Peterson, and R. S. Fearing, "Dash: A dynamic 16g hexapod robot," in *IEEE/RSJ Intl. Conf. on Intelligent Robots and Systems*. IEEE, 2009, pp. 2683–2689.
- [13] O. Ozcan, A. T. Baisch, D. Ithier, and R. J. Wood, "Powertrain Selection for a Biologically-Inspired Miniature Quadruped Robot," in *Review: IEEE Intl. Conf. on Robotics and Automation*, Hong Kong, China, 2014.
- [14] T. Kane and P. Mitiguy, "Motiongenesis-kane 5.2," 2011.
- [15] R. J. Wood, E. Steltz, and R. S. Fearing, "Optimal energy density piezoelectric bending actuators," *Sensors and Actuators A: Physical*, vol. 119, no. 2, pp. 476–488, 2005.
- [16] N. T. Jafferis, M. J. Smith, and R. J. Wood, "Design and manufacturing rules for maximizing the performance of polycrystalline piezoelectric bending actuators," *To appear: Smart Materials and Structures*, vol. 24, no. 6, p. 065023, 2015.
- [17] R. J. Wood, E. Steltz, and R. S. Fearing, "Nonlinear performance limits for high energy density piezoelectric bending actuators," in *ICRA*. IEEE, 2005, pp. 3633–3640.
- [18] A. T. Baisch, P. S. Sreetharan, and R. J. Wood, "Biologically-inspired locomotion of a 2g hexapod robot," in *IEEE/RSJ Intl. Conf. on Intelligent Robots and Systems*. IEEE, 2010, pp. 5360–5365.
- [19] R. Wood, S. Avadhanula, R. Sahai, E. Steltz, and R. Fearing, "Micro-robot design using fiber reinforced composites," *Journal of Mechanical Design*, vol. 130, p. 052304, 2008.
- [20] L. L. Howell, *Compliant mechanisms*. John Wiley & Sons, 2001.
- [21] DuPont, "Kapton® HN polyimide film," *Datasheet*, 2011.
- [22] S. H. Crandall, "The role of damping in vibration theory," *Journal of Sound and Vibration*, vol. 11, no. 1, pp. 3–IN1, 1970.
- [23] M. F. Ashby and D. Cebon, "Materials selection in mechanical design," *Le Journal de Physique IV*, vol. 3, no. C7, pp. C7–1, 1993.
- [24] M. Goldfarb and J. E. Speich, "A well-behaved revolute flexure joint for compliant mechanism design," *Journal of Mechanical Design*, vol. 121, no. 3, pp. 424–429, 1999.